Gas-Phase Organometallic Catalysis: Kinetics and Mechanism of the Hydrogenation of Ethylene by $Fe(CO)_3(C_2H_4)_2$

Michael E. Miller† and Edward R. Grant*

Contribution from the Department of Chemistry, Purdue University, West Lafayette, Indiana 47907. *Received April 21, 1987*

Abstract: Inert homogeneous gas-phase mixtures of ethylene and hydrogen plus a catalytic amount of $Fe(CO)_5$ are transformed into active ethylene hydrogenation systems upon irradiation by near-UV light from a pulsed nitrogen laser. Organometallic species present in the active catalytic mixture are identified and monitored by Fourier transform infrared spectroscopy. The catalyzed reaction is followed by gas chromatography, which provides a measure of ethylene and hydrogenated product concentrations. The catalytic process is efficient in its use of light, with typical room temperature quantum yields (product ethane molecules formed per photon absorbed) of 20 or more. The absorbed laser light generates a reservoir of $Fe(CO)_3(C_2H_4)_2$, which thermally dissociates by losing one highly labile ethylene to yield the active catalyst, $Fe(CO)_3(C_2H_4)$. When the photolysis light is removed, catalytic activity is observed to decline as the catalyst combines with free CO to form stable $Fe(CO)_4(C_2H_4)$. The rate of organic product formation is directly proportional to the catalyst reservoir concentration. Quantum efficiency of ethane production and the rate of $Fe(CO)_3(C_2H_4)_2$ decay are studied as functions of ethylene, hydrogen, CO, and $Fe(CO)_5$ pressures. The results provide information on the mechanism of catalysis, as well as elementary rate parameters for many of the organometallic reactions.

Iron carbonyls have long been noted as effective catalysts for the reactions of olefins and hydrogen. For example, under hydrogen pressure, heated solutions of various dienes with iron pentacarbonyl are observed to undergo hydrogenation reactions.[1,2] However, the thermal catalytic system is reactive only at temperatures above 160 °C and hydrogen pressures greater than 10 atm.[3] Double bond isomerization occurs along with hydrogenation, and the active system exhibits a complex set of additional catalytic reactions, including diene hydrogenation to monoene, monoene double bond shift, and monoene hydrogenation. IR spectra of samples removed from the reacting system reveal diene tricarbonyl and monoene tetracarbonyl iron complexes,[3] which implicate CO dissociation from $Fe(CO)_5$ as a likely first step.

Iron pentacarbonyl is also known for its rich photosubstitution chemistry,[4] which follows from CO photodissociation as the first step. It is thus not surprising that $Fe(CO)_5$ and its various derivatives make excellent room temperature olefin hydrogenation and isomerization photocatalysts.[5-10] Double bond isomerization accompanies hydrogenation whenever chemically possible, indicating a common organometallic catalytic species for both processes. Neat 1-pentene solutions afford product quantum yields as high as 4 for hydrogenation and 800 for isomerization.[6] These large quantum yields indicate the photogeneration of a highly reactive thermal catalyst.

No elementary rate data exist for these liquid-phase photocatalytic systems. Only overall rates and quantum yields have been measured, which have sometimes proven difficult to reproduce.[8] A coordinatively unsaturated catalyst has never been observed, but iron tricarbonyl has been proposed as the repeating unit in the catalytic cycle.[5,6] Recent in situ infrared spectral measurements have identified thermally labile bisolefin iron tricarbonyls as observable catalytically important species.[11,12]

In liquid solutions, solvent interactions are impossible to avoid. For example, attempts to generate unsaturated $W(CO)_5$ in solution have produced only $W(CO)_5$(solvent) as a detectable product,[13] while $Cr(CO)_5$ fragments are found to combine with solvent molecules within 25 ps.[14] Thus it seems appropriate to look to the gas phase in an effort to find a simpler picture of the reactions that make up the photocatalytic iron carbonyl olefin transformation systems.

The first gas-phase photocatalytic organometallic system was demonstrated in our own laboratories by Whetten et al.[15] This work found hydrogenation and double bond isomerization of 1-pentene upon UV laser irradiation of mixtures of this substrate, hydrogen, and iron pentacarbonyl. Photocatalysis in this system is highly efficient, with quantum yields up to 18 for hydrogenation and 220 for isomerization. Without hydrogen, the isomerization occurs alone, exhibiting higher quantum efficiencies.

Ethylene is the simplest molecule containing a carbon–carbon double bond. As a substrate in the $H_2/Fe(CO)_5$ photocatalytic system, ethylene isolates hydrogenation. Indeed, we find that ultraviolet laser irradiation of gaseous mixtures of ethylene, hydrogen, and $Fe(CO)_5$ yields ethane as the only organic product.[16-18]

The following is a thorough spectroscopic and kinetic study, which provides elementary data on this simplest photocatalytic hydrogenation reaction. The results constitute the first detailed set of measurements for such a system in the gas phase.

Results

Catalytic mixtures in Pyrex reaction cells are irradiated and analyzed for ethane product yield by flame ionization gas chromatography. A typical sample contains 0.50 Torr of $Fe(CO)_5$, 3.0 Torr of CO, 400 Torr of C_2H_4, and 1000 Torr of H_2. The catalytic system is extremely air-sensitive, with very small air levels (≥20 ppm) dramatically reducing the product yield and reaction efficiency.

The usual laser repetition rate is 4 Hz. Catalysis is initiated

† Present address: Department of Agronomy, 726 Bradfield Hall, Cornell University, Ithaca, NY 14853.

(1) Frankel, E. N.; Enken, E. A.; Peters, H. M.; Davison, V. L.; Butterfield, R. O. *J. Org. Chem.* **1964**, *29*, 3292.
(2) Frankel, E. N.; Enken, E. A.; Davison, V. L. *J. Org. Chem.* **1965**, *30*, 2739.
(3) Cais, M.; Moaz, N. *J. Chem. Soc. A* **1971**, 1811.
(4) Geoffroy, G. L.; Wrighton, M. S. *Organometallic Photochemistry*; Academic: New York, 1979.
(5) Schroeder, M. A.; Wrighton, M. S. *J. Am. Chem. Soc.* **1976**, *98*, 551.
(6) Whetten, R. L.; Fu, K.-J.; Grant, E. R. *J. Am. Chem. Soc.* **1982**, *104*, 4270.
(7) Sanner, R. D.; Austin, R. G.; Wrighton, M. S.; Honnick, W. D.; Pittman, C. U., Jr. *Inorg. Chem.* **1979**, *18*, 928.
(8) Swartz, G. L.; Clark, R. J. *Inorg. Chem.* **1980**, *19*, 3191.
(9) Mitchener, J. C.; Wrighton, M. S. *J. Am. Chem. Soc.* **1981**, *103*, 975.
(10) Graff, J. L.; Sanner, R. D.; Wrighton, M. S. *Organometallics* **1982**, *1*, 837.
(11) Fleckner, H.; Grevels, F.-W.; Hess, D. *J. Am. Chem. Soc.* **1984**, *106*, 2027.
(12) Wuu, Y.-M.; Bentsen, J. G.; Brinkley, C. G.; Wrighton, M. S. *Inorg. Chem.* **1987**, *26*, 530.
(13) Lees, A. J.; Adamson, A. W. *Inorg. Chem.* **1981**, *20*, 4381.
(14) Welch, J. A.; Peters, K. S.; Vaida, V. *J. Phys. Chem.* **1982**, *86*, 1941.
(15) Whetten, R. L.; Fu, K.-J.; Grant, E. R. *J. Chem. Phys.* **1982**, *77*, 3769.
(16) Miller, M. E.; Grant, E. R. *Proc. Soc. Photo Opt. Instrum. Eng.* **1984**, *458*, 154.
(17) Miller, M. E.; Grant, E. R. *J. Am. Chem. Soc.* **1984**, *106*, 4635.
(18) Miller, M. E.; Grant, E. R. *J. Am. Chem. Soc.* **1985**, *107*, 3386.

0002-7863/87/1509-7951$01.50/0

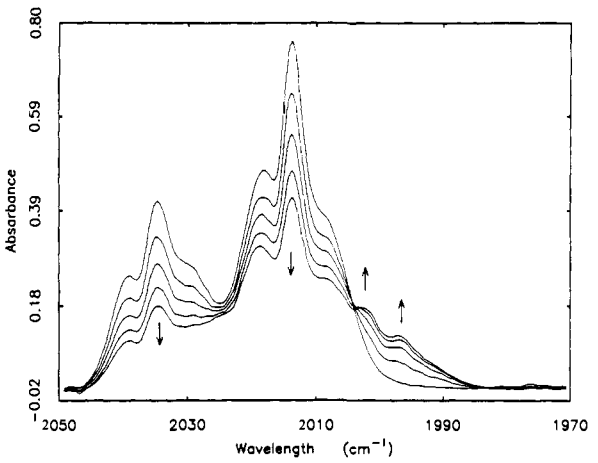

Figure 1. FTIR spectra of the irradiated catalytic system at room temperature and with a laser repetition rate of 4 Hz. The spectra are recorded at 0, 10, 20, 30, and 40 min irradiation time. Arrows indicate the direction of change. The constant background spectrum of CO and ethylene has been subtracted from each. Initial pressures inside the 281.7 mL, 16.2 cm path length T-cell: 0.10 Torr of $Fe(CO)_5$, 3.0 Torr of CO, 400 Torr of C_2H_4, and 506 Torr of H_2.

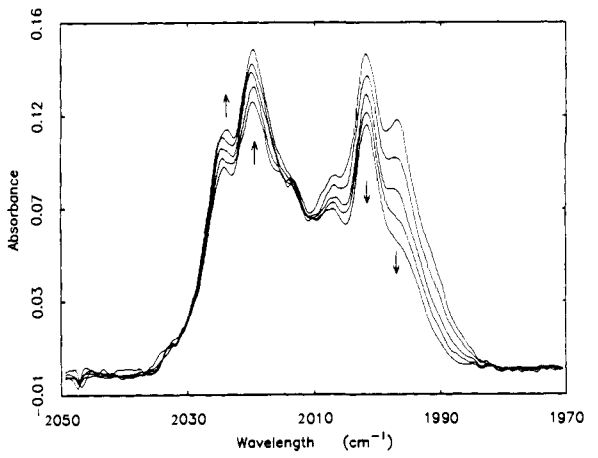

Figure 2. Time-dependent FTIR spectra of the catalytic system, after laser irradiation, minus the $Fe(CO)_5$ spectrum. Spectra are recorded 0, 6, 13, 23, and 95 min after irradiation. Arrows denote the direction of change.

by unfocussed laser light, with no reaction occurring in the dark. Iron pentacarbonyl absorbs strongly in the ultraviolet region and exhibits a long absorbance tail extending into the visible with a molar extinction coefficient of 260 at the nitrogen laser wavelength, 337 nm. Since the other components of the catalytic mixture do not absorb in the near-UV, the laser light excites only the iron carbonyl species.

In experiments to observe intermediate iron carbonyls, catalytic mixtures are irradiated within the sample chamber of an FTIR spectrometer, where organometallic species are monitored by their absorptions in the carbonyl stretch region (2200–1700 cm^{-1}).

FTIR carbonyl stretch spectra of a catalytic mixture (with CO and C_2H_4 subtracted out) during a laser irradiation period of 50 min are shown in Figure 1. Inspection of these spectra reveals bands at 2002 and 1997 cm^{-1} growing in at the expense of $Fe(CO)_5$ absorptions. Figure 2 shows the final irradiated spectrum *minus* the scaled initial $Fe(CO)_5$ spectrum. The absorption bands of the photogenerated species are uncovered by this subtraction: 2024, 2020, 2007, 2002, and 1997 cm^{-1}.

After the laser light is removed, further IR spectral changes occur in the dark, as also shown in Figure 2. $Fe(CO)_5$ absorption intensities remain essentially constant, while the bands at 2024 and 2020 cm^{-1} increase in intensity, and those at 2002 and 1997 cm^{-1} diminish.

A recent, detailed kinetic study of the iron carbonyl–ethylene system[19] yields an unambiguous assignment of these evolving

Table I. Gas-Phase FTIR Bands of Substituted Iron Carbonyls as Confirmed by Kinetic Spectroscopy[19]

complex	frequencies, cm^{-1} (ϵ or rel absorbance)[a]
$Fe(CO)_5$	2039, (2960, sh); 2034 (4910); 2018 (5940, sh); 2014 (9450); 1976 (200); 645 (1090); 619 (370); 473 (140); 423 (130)
$Fe(CO)_4(C_2H_4)$	2100 (290, sh); 2095 (570); 2024 (3850, sh); 2020 (5180); 2007 (2590); 2002 (3880); 1967 (98); 1194 (100); 706 (30); 636 (760); 592 (210); 494 (110); 458 (43)
$Fe(CO)_3(C_2H_4)_2$[b]	2069 (390); 2001 (4280); 1997 (5340); 1967 (140); 1198 (220); 715 (130); 628 (390)
$Fe(CO)_4(H)_2$	2125 (99); 2066 (sh); 2057 (4000); 2052 (5510); 2046 (sh); 2014 (220); 800 (180); 764 (94); 695 (240); 609 (180); 583 (150)
$Fe(CO)_4(D_2)$	2125 (0.018); 2066 (sh); 2056 (0.752); 2052 (1.00); 2048 (sh); 2014 (0.102); 768 (0.018); 720 (0.014); 684 (0.037); 649 (0.083); 612 (0.019)

[a] ϵ/L mol^{-1} cm^{-1}; sh = shoulder. [b] Most low-frequency bands are obscured in our system by strong ethylene absorptions.

features. As listed in Table I, bands at 2024, 2020, 2007, and 2002 cm^{-1} can be associated with $Fe(CO)_4(C_2H_4)$, while subtraction of the $Fe(CO)_4(C_2H_4)$ carbonyl spectrum leaves only the 2001- and 1997-cm^{-1} absorptions of $Fe(CO)_3(C_2H_4)_2$. Thus irradiation of the catalytic mixture generates monoethylene iron tetracarbonyl and bisethylene iron tricarbonyl. Irradiation of $Fe(CO)_5$ in the presence of H_2 alone produces $Fe(CO)_4(H)_2$, as established by characteristic carbonyl peaks at 2057 and 2052 cm^{-1}, as well as Fe–H stretches.[20] No $Fe(CO)_4(H)_2$ is detected in catalytic mixtures, nor is significant catalytic hydrogenation observed when ethylene is added to photoprepared gas-phase $Fe(CO)_4(H)_2$.

After irradiation, bands due to $Fe(CO)_3(C_2H_4)_2$ decrease and eventually disappear as the $Fe(CO)_4(C_2H_4)$ absorptions increase in intensity. These changes are linearly related, indicating that the overall reaction of eq 1 occurs in the dark following irradiation.

$$Fe(CO)_3(C_2H_4)_2 + CO \rightarrow Fe(CO)_4(C_2H_4) + C_2H_4 \quad (1)$$

The molar extinction coefficients for $Fe(CO)_3(C_2H_4)_2$ are calculated from the ratio of absorbance changes between successive spectra after irradiation (2020 cm^{-1} for $Fe(CO)_4(C_2H_4)$ and 1997 cm^{-1} for $Fe(CO)_3(C_2H_4)_2$) and from the measured ϵ for $Fe(CO)_4(C_2H_4)$ at 2020 cm^{-1} (see Table I). The decay of the bisethylene complex (eq 1) is enhanced by increasing the CO or H_2 pressures and is inhibited by increasing the ethylene pressure.

If a mixture of CO, ethylene, and hydrogen, plus a small amount of $Fe(CO)_5$ or $Fe(CO)_4(C_2H_4)$, is left in the dark, no ethane is produced as detected by gas chromatography. When hydrogen is added to a photochemicaly produced mixture of $Fe(CO)_3(C_2H_4)_2$ and ethylene, very efficient formation is observed with a final ethane to initial $Fe(CO)_3(C_2H_4)_2$ mole ratio greater than 50:1.

Following irradiation of the catalytic mixture, we observe the formation of ethane and the decay of $Fe(CO)_3(C_2H_4)_2$ to take place at the same first-order rate. More precisely, the degree of completion of the reaction, as measured by the mole fraction of ethane produced divided by the final amount of ethane, or as measured by $1-[Fe(CO)_3(C_2H_4)_2]/[Fe(CO)_3(C_2H_4)_2]_0$, follows the same $(1 - e^{-kt})$ time dependence, as shown in Figure 3. Thus the rate of ethane production is directly proportional to the $Fe(CO)_3(C_2H_4)_2$ concentration.

The product quantum yield, Φ, is defined as the number of organic product (ethane) molecules formed per photon absorbed by the reaction mixture. This number is a measure of photocatalytic efficiency and is used to characterize the ethylene hydrogenation system. Most quantum yield measurements are made

(19) Weiller, B. H.; Miller, M. E.; Grant, E. R. *J. Am. Chem. Soc.* **1987**, *109*, 1051.
(20) Stobart, S. R. *J. Chem. Soc., Dalton Trans.* **1972**, 2442.

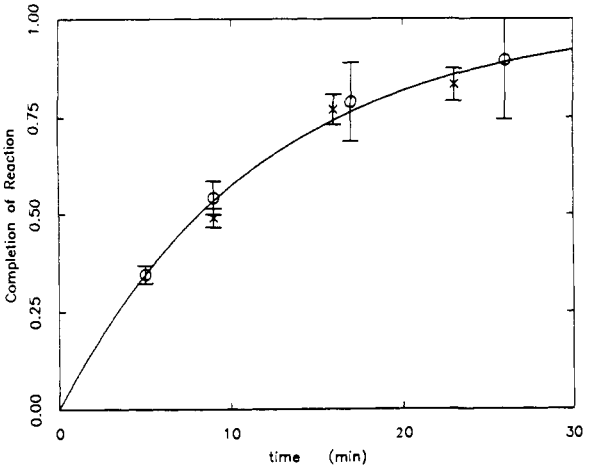

Figure 3. Completion of reaction vs time after irradiation of the catalytic system at room temperature, measured by X_{ethane}/X_∞(crosses) and 1-$[Fe(CO)_3(C_2H_4)_2]/[Fe(CO)_3(C_2H_4)_2]_0$ (open circles). Initial pressures: 0.30 Torr of $Fe(CO)_5$, 3.0 Torr of CO, 300 Torr of C_2H_4, 600 Torr of H_2. The curve is $y = 1 - e^{-kt}$ with $k = 0.085$ min^{-1}.

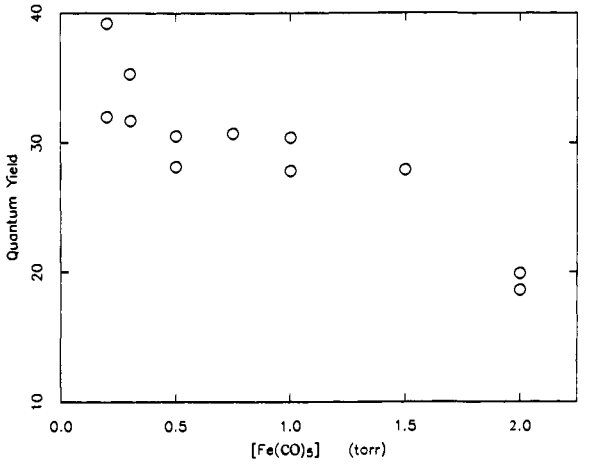

Figure 4. Quantum yield as a function of $[Fe(CO)_5]$ at 43 °C and 4 Hz laser repetition rate. Initial pressures: 3.0 Torr of CO, 400 Torr of C_2H_4, 1000 Torr of H_2.

at 43 °C, a temperature at which the hydrogenation occurs at a conveniently fast rate.

Figure 4 shows the effects of increasing the initial pressure of $Fe(CO)_5$. Catalysis becomes *less* efficient as more iron pentacarbonyl is added to the reaction mixture, ruling out the possibility of catalysis by iron clusters.[21] If the initial iron pentacarbonyl pressure is greater than about 1.5 Torr, adverse clustering reactions become so favorable that an orange film can be seen on the cell walls after irradiation.

As the laser pulse repetition rate is increased, keeping the energy per pulse constant, the power incident on the reaction mixture increases, and a loss in catalytic efficiency is observed. If the laser repetition rate is increased, *with the average power held constant*, the quantum yield shows no repetition rate dependence. These complementary results imply that the observed decline in Φ is caused by an increasing number of photogenerated organometallic species, which react with each other in preference to the substrates, rather than a laser pulse perturbation of catalytic cycles previously hypothesized.[18]

The quantum yield for ethane production falls dramatically with increasing carbon monoxide pressure (cf. Figure 5). This decrease is systematic and follows the inverse dependence illustrated in Figure 6. Although added CO degrades the photocatalytic efficiency, a small amount is necessary to ensure the reproducibility of measured quantum yields. We observe that the added CO effectively competes with clustering reactions, keeping the system clean.

Increasing the pressure of either hydrogenation substrate, ethylene or hydrogen, causes the quantum yield to increase and approach an asymptotic maximum as shown in Figures 7 and 8. Figure 8 also compares hydrogenation and deuteriation at 43 °C.

(21) Laine, R. M. *J. Mol. Catal.* **1982**, *14*, 137.

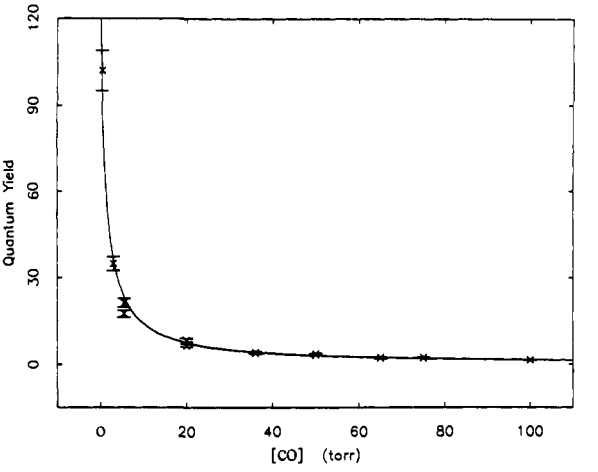

Figure 5. Quantum yield as a function of CO pressure at 43 °C and 4 Hz. Initial pressures: 0.5 Torr of $Fe(CO)_5$, 400 Torr of C_2H_4, 1400 Torr of H_2. The error bars indicate an uncertainty in Φ of ±7%. The curve is derived from a linear fit of $1/\Phi$ vs [CO] (see Figure 6).

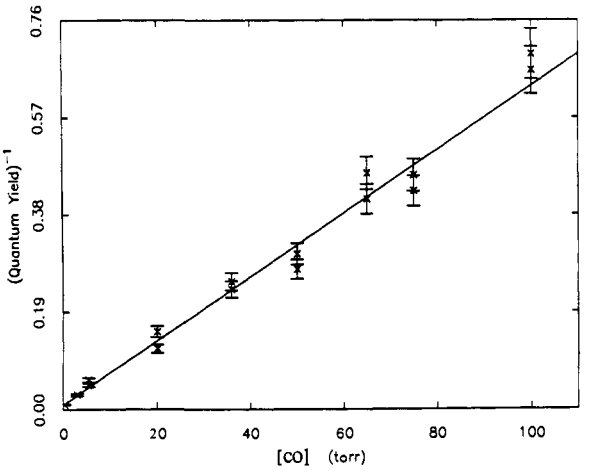

Figure 6. Inverse quantum yield vs CO pressure. The data are taken from the experiments shown in Figure 5. The line is the best weighted linear least-squares fit to the data.

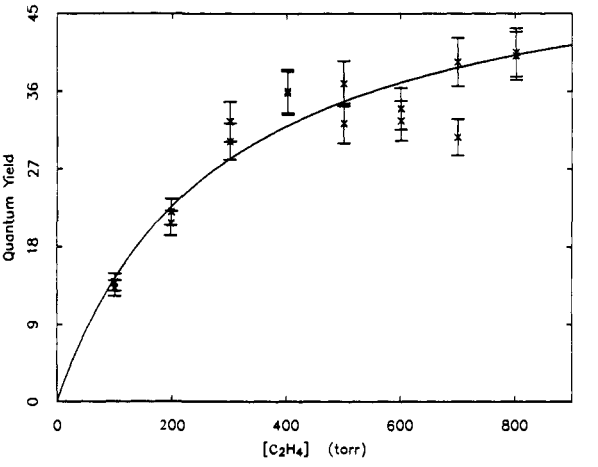

Figure 7. Quantum yield as a function of ethylene pressure at 43 °C and 4 Hz. Initial pressures: 0.5 Torr of $Fe(CO)_5$, 3.0 Torr of CO, 800 Torr of H_2. The error bars indicate an uncertainty in Φ of ±7%. The curve is a fit to the form derived in the text as eq 49.

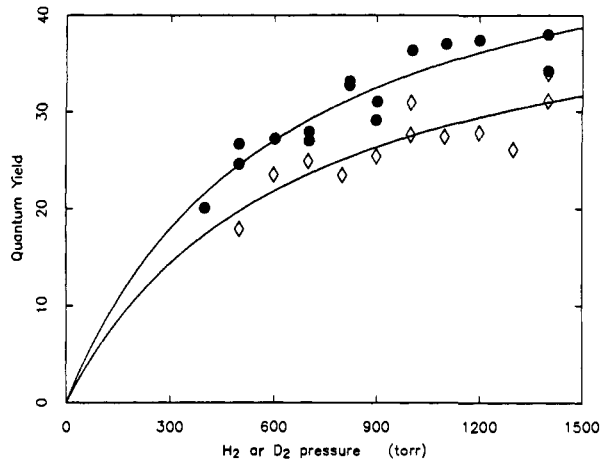

Figure 8. Quantum yield as a function of $[H_2]$ (solid circles) and $[D_2]$ (open diamonds) at 43 °C and 4 Hz. Initial pressures: 0.5 Torr of $Fe(CO)_5$, 3.0 Torr of CO, 400 Torr of C_2H_4. The curves are fit to the form derived in the text as eq 49.

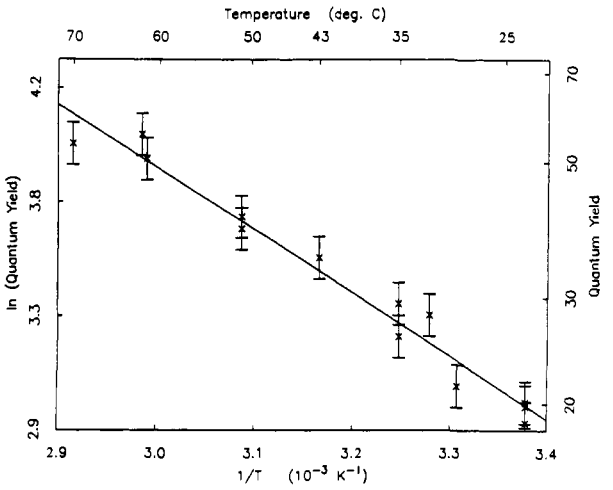

Figure 9. Temperature dependence of the quantum yield with a laser repetition rate of 4 Hz. Initial pressures: 0.5 Torr of $Fe(CO)_5$, 3.0 Torr of CO, 400 Torr of C_2H_4, 1400 Torr of H_2. The error bars indicate an uncertainty in Φ of ±7%. The line is a linear least-squares fit of ln Φ vs $1/T$.

Over the measured pressure range, the quantum yield ratio is constant within the experimental uncertainty at $\Phi_H/\Phi_D = 1.2 \pm 0.1$. At room temperature (23 °C) and 1400 Torr of H_2 and D_2, the ratio is about 1.3.

The quantum yield increases with increasing temperature, displaying the Arrhenius-like behavior shown in Figure 9 for the range of 23–70 °C. What may be termed an overall activation energy is obtained from the slope of the Arrhenius plot: 4.7 ± 0.3 kcal/mol.

Discussion

Sequence of Reactions in Gas-Phase Photocatalytic Hydrogenation. Following irradiation of reaction mixtures of ethylene, hydrogen, carbon monoxide, and a small amount of $Fe(CO)_5$, changes in the carbonyl FTIR spectrum are characterized by the appearance of features assigned to the ethylene-substituted complexes, $Fe(CO)_4(C_2H_4)$ and $Fe(CO)_3(C_2H_4)_2$, the latter of which is associated kinetically with catalytic activity.

Pathways for this photoinitiation process, accessible by absorption of 337-nm photons, are detailed in Figure 10.[22] The mechanism proposed for propagation of hydrogenation catalysis,

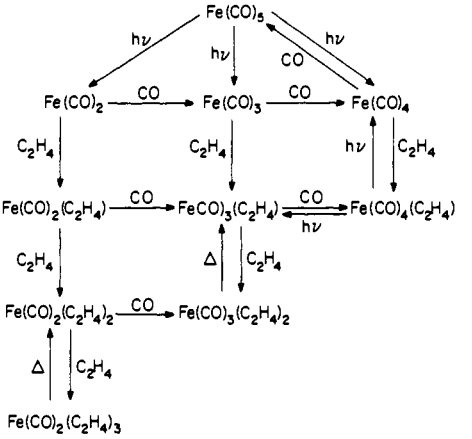

Figure 10. Photolysis mechanism for irradiation of the catalytic mixture by 337-nm laser light.

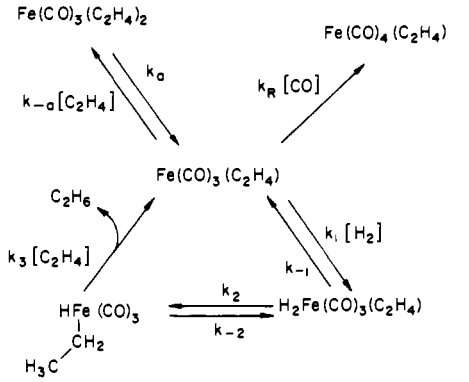

Figure 11. Catalytic mechanism for ethylene hydrogenation with $Fe(CO)_3(C_2H_4)_2$.

after a substantial irradiation period, is illustrated in Figure 11. It is rationalized as follows. Substitution processes in iron carbonyl complexes generally proceed through a dissociative pathway.[23,24] Thus we hypothesize that the unstable bisethylene complex thermally decomposes by loss of one ethylene ligand to yield $Fe(CO)_3(C_2H_4)$. This 16-electron complex provides entry into the catalytic cycle by reversible oxidative addition of H_2, producing the coordinatively saturated complex, $H_2Fe(CO)_3(C_2H_4)$. Such hydrogen additions are commonly encountered in coordinatively unsaturated, d^8 complexes such as $Fe(CO)_3(C_2H_4)$.[25] Alternatively, the addition of H_2 to the iron carbonyl fragments, $Fe(CO)_{5-n}$, would eventually yield $H_2Fe(CO)_4$, which we do not see.

Isolable complexes containing both hydride and olefin ligands are quite rare, because hydride migration is so favorable.[25] Thus, the most probable next step for $H_2Fe(CO)_3(C_2H_4)$ is reversible migratory insertion of a hydride to form the 16-electron ethyl complex, $HFe(CO)_3(C_2H_5)$. In a few rare cases hydride-olefin insertion has been directly observed,[26,27] with the reverse reaction having been studied in an iron carbonyl system.[28] A second hydride insertion to yield the product ethane, when driven by ethylene addition, takes the cycle back to the catalyst, $Fe(CO)_3(C_2H_4)$.

Wilkinson's hydrogenation catalyst, $H_2RhCl(PPh_3)_3$, which has been carefully studied by Halpern et al.,[29] acts much as $H_2Fe(CO)_3(C_2H_4)$ is proposed to behave. In the case of Wilkinson's catalyst, the second hydride insertion to yield organic product is

(22) Engelking, P. C.; Lineberger W. C. *J. Am. Chem. Soc.* **1979**, *101*, 5569. Yardley, J. T.; Gitlin, B.; Nathanson, G.; Rosan, A. M. *J. Chem. Phys.* **1981**, *74*, 370. Fu, K. J.; Whetten, R. L.; Grant, E. R. *Ind. Eng. Chem. Prod. Res. Dev.* **1984**, *23*, 33.

(23) Cardaci, G.; Narciso, V. *J. Chem. Soc., Dalton Trans.* **1972**, 2289.
(24) Burkinshaw, P. M.; Dixon, D. T.; Howell, J. A. S. *J. Chem. Soc., Dalton Trans.* **1980**, 999.
(25) See, for example: Collman, J. P.; Hegedus, L. S. *Principles and Applications of Organotransition Metal Chemistry*; University Science Books: Mill Valley, CA, 1980.
(26) Werner, H.; Feser, R. *Angew. Chem., Int. Ed. Engl.* **1979**, *18*, 157.
(27) Roe, D. C. *J. Am. Chem. Soc.* **1983**, *105*, 7770.
(28) Kazlauskas, R. J.; Wrighton, M. S. *Organometallics* **1982**, *1*, 602.
(29) Halpern, J.; Okamoto, T.; Zakhariev, A. *J. Mol. Catal.* **1976**, *2*, 65.

very fast, with the first insertion suggested to be rate-determining. Halpern also observes a small deuterium isotope effect on the catalytic rate of 1.15, which is comparable to our measured ratio of $\Phi_H/\Phi_D = 1.3$. Finally, we note that the $Fe(CO)_5$ photocatalytic hydrogenation cycle proposed by Figure 11 is propogated by iron tricarbonyl complexes, as was suggested by Schroeder and Wrighton[5] and by Whetten et al.[6]

In this mechanism, CO addition is responsible for irreversible loss of the catalyst, $Fe(CO)_3(C_2H_4)$, by forming stable $Fe(CO)_4(C_2H_4)$. By this route, catalytic activity decays to zero in the time interval following irradiation. The bisethylene complex, $Fe(CO)_3(C_2H_4)_2$, acts as a reservoir for the catalyst. Ethylene pushes the equilibrium toward this reservoir, slowing down catalysis, but not decreasing the final product yield, since all $Fe(CO)_3(C_2H_4)_2$ must eventually pass through the coordinatively unsaturated catalyst before CO deactivation. In the previous section, we found the rate of ethane production to be directly proportional to the concentration of $Fe(CO)_3(C_2H_4)_2$. This proportionality can thus be seen as a direct consequence of the equilibrium between the bisethylene complex and the hydrogenation catalyst.

FTIR kinetic studies provide further detail on the $Fe(CO)_5$ photocatalyzed hydrogenation mechanism. As we have seen, bisethylene iron tricarbonyl is unstable with respect to ethylene loss and is not observed in the absence of excess ethylene. Once formed in the catalytic system, $Fe(CO)_3(C_2H_4)_2$ undergoes a substitution reaction with carbon monoxide to yield monoethylene iron tetracarbonyl (eq 1). The elementary mechanism is that of dissociative substitution (cf. Figure 11).

Spectroscopic analysis of reaction rates as a function of CO and C_2H_4 pressures, in noncatalytic systems containing only $Fe(CO)_4(C_2H_4)$, $Fe(CO)_3(C_2H_4)_2$, CO, and C_2H_4, yield values for k_a, the unimolecular dissociation rate of $Fe(CO)_3(C_2H_4)_2$, and k_R/k_{-a}, the room temperature branching ratio for recombination of $Fe(CO)_3(C_2H_4)$ with CO versus ethylene.[19] The average values are $k_a = 0.17 \pm 0.02$ min^{-1} and $k_R/k_{-a} = 35 \pm 5$.

More recently we have conducted additional determinations k_a and k_R/k_{-a} at a single elevated temperature of 43 °C.[30] We find $k_a = 2.6 \pm 1.6$ min^{-1} and $k_R/k_{-a} = 16 \pm 10$. The smaller branching ratio at a higher temperature indicates an activation energy difference for the CO versus ethylene recombination with $Fe(CO)_3(C_2H_4)$. From a crude, two-point Arrhenius dependence, we estimate an energy difference of $E_{-a} - E_R = 8 \pm 6$ kcal/mol. We must thus conclude that a barrier exists for ethylene recombination, and perhaps also for recombination with CO.

A two-point fit of the k_a values to the Arrhenius equation provides an estimate for the dissociation energy of $Fe(CO)_3(C_2H_4)_2$ of 27 ± 6 kcal/mol, with an A factor of 10^{17} ($\Delta S^{\ddagger} \simeq 20$ eu). This activation energy falls within the range of values measured by Cardaci and Narciso for the loss of monosubstituted ethylenes from various metastable monoolefin iron tetracarbonyl complexes:[23]

$$Fe(CO)_4(\text{olefin}) \rightarrow Fe(CO)_4 + \text{olefin}$$

These authors also observe a small temperature dependence for the branching ratio of CO versus olefin recombination with $Fe(CO)_4$. Both of their results lend confidence to our estimated energy parameters.

Hydrogen-Promoted Deactivation of Catalyst. When a mixture of $Fe(CO)_4(C_2H_4)$, CO, ethylene, and hydrogen is irradiated by 337-nm laser light, substantial conversion to $Fe(CO)_3(C_2H_4)_2$ occurs along with efficient ethylene hydrogenation. In the dark, the system relaxes back to $Fe(CO)_4(C_2H_4)$, displaying the same spectral changes observed in the system without hydrogen. In addition, plots of carbonyl absorbance changes, $\ln |A - A_\infty|$, versus time are linear for both monoethylene formation and bisethylene decay, all of which indicates a clean conversion to $Fe(CO)_4(C_2H_4)$ as expressed by eq 1. However, as shown by Figure 12, values of the observed rate constant (k_{obsd}) depend on the hydrogen pressure, increasing with increasing $[H_2]$. This behavior cannot be predicted from the catalytic mechanism outlined in Figure 11.

(30) Miller, M. E.; Grant, E. R., unpublished results. Methods and data sets are of the same form as room temperature determinations. A complete account of these results will be included in a report on the wider temperature dependence of this reaction together with those associated with dissociative CO substitutions in $Fe(CO)_4(C_2H_4)$ and $Cr(CO)_5(C_2H_4)$.

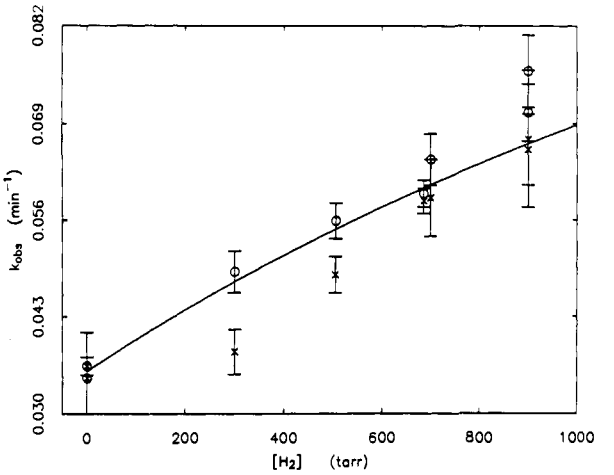

Figure 12. Hydrogen pressure dependence of k_{obsd} at 24 °C. Open circles are measured from $Fe(CO)_3(C_2H_4)_2$ decay and crosses are from $Fe(CO)_4(C_2H_4)$ formation. The curve is the best, weighted non-linear least-squares fit to the reciprocal of eq 23. Initial pressures: 0.10 Torr of $Fe(CO)_4(C_2H_4)$, 3.0 Torr of CO, 400 Torr of C_2H_4.

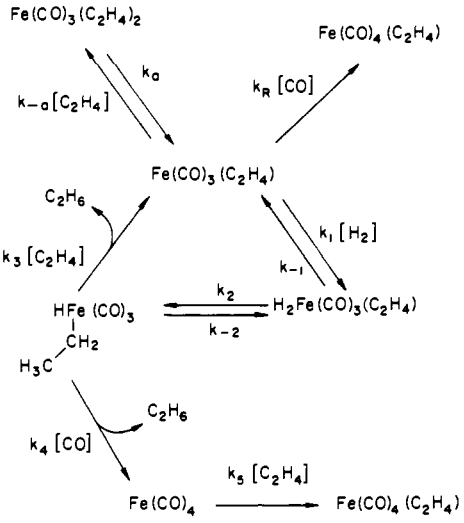

Figure 13. Complete mechanism for the hydrogenation of ethylene in the presence of $Fe(CO)_3(C_2H_4)_2$.

A closer look at the catalytic mechanism in Figure 11, which is evidently incomplete, reveals a likely branch point. We have assumed so far that the 16-electron monohydride ethyl complex $HFe(CO)_3(C_2H_5)$ is induced to liberate ethane by the attack of an ethylene molecule, which takes the iron tricarbonyl fragment back to catalyst, $Fe(CO)_3(C_2H_4)$. At this stage, however, monohydride ethyl iron tricarbonyl can also be intercepted by a carbon monoxide molecule. This latter path also liberates the product ethane, but it takes the iron to $Fe(CO)_4$, which then is very likely to irreversibly bind ethylene, providing a second deactivation route to the stable monoethylene complex. The expanded catalytic mechanism is presented in Figure 13. It seems unlikely that $HFe(CO)_3(C_2H_5)$ is also intercepted by hydrogen, since this channel would generate some $H_2Fe(CO)_4$, which we do not observe in the catalytic system.

This second deactivation pathway is actually promoted by hydrogen, since the hydrogenation cycle is initiated by oxidative addition of H_2 to $Fe(CO)_3(C_2H_4)$. The cycle leads to the branch species $HFe(CO)_3(C_2H_5)$, from which the stable monoethylene complex is generated a certain fraction of the time. Thus, the mechanism for bisethylene iron tricarbonyl decay in the presence of hydrogen is formulated as follows:

$$Fe(CO)_3(C_2H_4)_2 \xrightarrow{k_a} Fe(CO)_3(C_2H_4) + C_2H_4 \quad (2)$$

$$Fe(CO)_3(C_2H_4) + C_2H_4 \xrightarrow{k_{-a}} Fe(CO)_3(C_2H_4)_2 \quad (3)$$

$$Fe(CO)_3(C_2H_4) + CO \xrightarrow{k_R} Fe(CO)_4(C_2H_4) \quad (4)$$

$$Fe(CO)_3(C_2H_4) + H_2 + CO + C_2H_4 \rightarrow Fe(CO)_4(C_2H_4) + C_2H_6 \quad (5)$$

Equation 5 is not an elementary reaction, but it encompasses the catalytic hydrogenation cycle, with an exit leading from $HFe(CO)_3(C_2H_5)$ to the monoethylene complex. The rate equation for monoethylene complex formation from within the catalytic cycle via $HFe(CO)_3(C_2H_5)$ is provided by the mechanism of Figure 13.

$$d[Fe(CO)_4(C_2H_4)]/dt = k_5[C_2H_4][Fe(CO)_4] \quad (6)$$

Application of the steady-state assumption to the concentrations of the intermediates $Fe(CO)_4$, $HFe(CO)_3(C_2H_5)$, and $H_2Fe(CO)_3(C_2H_4)$ allows them all to be expressed in terms of the catalyst concentration, $[Fe(CO)_3(C_2H_4)]$:

$$k_5[C_2H_4][Fe(CO)_4] = k_4[CO][HFe(CO)_3(C_2H_5)] \quad (7)$$

$$[HFe(CO)_3(C_2H_5)] = \frac{k_2}{k_3[C_2H_4] + k_4[CO] + k_{-2}}[H_2Fe(CO)_3(C_2H_4)] \quad (8)$$

$$[H_2Fe(CO)_3(C_2H_4)] = \frac{k_{-2}[HFe(CO)_3(C_2H_5)] + k_1[H_2][Fe(CO)_3(C_2H_4)]}{k_2 + k_{-1}} \quad (9)$$

Substitution of eq 8 for $[HFe(CO)_3(C_2H_5)]$ into eq 9 gives $[H_2Fe(CO)_3(C_2H_4)]$ in terms of $[Fe(CO)_3(C_2H_4)]$:

$$[H_2Fe(CO)_3(C_2H_4)] = \frac{k_1[H_2](k_3[C_2H_4] + k_4[CO] + k_{-2})}{(k_2 + k_{-1})(k_3[C_2H_4] + k_4[CO]) + k_{-1}k_{-2}}[Fe(CO)_3(C_2H_4)] \quad (10)$$

Then application of eq 10 to eq 8 provides $[HFe(CO)_3(C_2H_5)]$ in terms of $[Fe(CO)_3(C_2H_4)]$.

$$[HFe(CO)_3(C_2H_5)] = \frac{k_1k_2[H_2]}{(k_2 + k_{-1})(k_3[C_2H_4] + k_4[CO]) + k_{-1}k_{-2}}[Fe(CO)_3(C_2H_4)] \quad (11)$$

Returning to the rate expression for monoethylene formation (eq 6), we substitute eq 7 and then 11 to obtain

$$\frac{d[Fe(CO)_4(C_2H_4)]}{dt} = \frac{k_1k_2k_4[CO][H_2]}{(k_2 + k_{-1})(k_3[C_2H_4] + k_4[CO]) + k_{-1}k_{-2}}[Fe(CO)_3(C_2H_4)] \quad (12)$$

The final result is of the form

$$d[Fe(CO)_4(C_2H_4)]/dt = k_b[H_2][Fe(CO)_3(C_2H_4)] \quad (13)$$

where

$$k_b = \frac{k_1k_2k_4[CO]}{(k_2 + k_{-1})(k_3[C_2H_4] + k_4[CO]) + k_{-1}k_{-2}} \quad (14)$$

The simple first-order dependence on hydrogen and catalyst concentrations motivates us to express the hydrogen-promoted deactivation, eq 5, as if it were an elementary process

$$Fe(CO)_3(C_2H_4) + H_2 \xrightarrow{k_b} Fe(CO)_4(C_2H_4) + C_2H_6 \quad (15)$$

where k_b contains the additional species (CO and C_2H_4) necessary to chemically balance the equation. The composite rate, k_b, depends parametrically on the ethylene and CO pressures, but it is constant under a particular set of experimental conditions, since these species are always present in large excess.

We now return to the mechanism for $Fe(CO)_3(C_2H_4)$ decay, as detailed by eq 2–5 with eq 15, and solve for k_{obsd} as a function of hydrogen pressure. Steady-state treatment of the catalyst concentration, $[Fe(CO)_3(C_2H_4)]$, gives

$$[Fe(CO)_3(C_2H_4)] = \frac{k_a[Fe(CO)_3(C_2H_4)_2]}{k_{-a}[C_2H_4] + k_R[CO] + k_b[H_2]} \quad (16)$$

The rate of $Fe(CO)_3(C_2H_4)_2$ decay is

$$-d[Fe(CO)_3(C_2H_4)_2]/dt = k_a[Fe(CO)_3(C_2H_4)_2] - k_{-a}[C_2H_4][Fe(CO)_3(C_2H_4)] \quad (17)$$

And the rate of $Fe(CO)_4(C_2H_4)$ formation is

$$d[Fe(CO)_4(C_2H_4)]/dt = (k_R[CO] + k_b[H_2])[Fe(CO)_3(C_2H_4)] \quad (18)$$

The steady-state assumption equates the rate of bisethylene decay to the rate of monoethylene formation. Substitution of eq 16 for the intermediate $[Fe(CO)_3(C_2H_4)]$ into eq 17 yields an expression for the decay rate of $Fe(CO)_3(C_2H_4)_2$:

$$-\frac{d[Fe(CO)_3(C_2H_4)_2]}{dt} = \frac{k_a(k_R[CO] + k_b[H_2])[Fe(CO)_3(C_2H_4)_2]}{k_{-a}[C_2H_4] + k_R[CO] + k_b[H_2]} \quad (19)$$

$$= k_{obsd}[Fe(CO)_3(C_2H_4)_2] \quad (20)$$

Thus the pseudo-first-order rate constant for bisethylene decay and monoethylene growth is given by the equation

$$k_{obsd} = \frac{k_a(k_R[CO] + k_b[H_2])}{k_{-a}[C_2H_4] + k_R[CO] + k_b[H_2]} \quad (21)$$

where the rate constant k_b is given by eq 14. Equation 21 predicts that k_{obsd} will increase with increasing hydrogen pressure, approaching an asymptotic maximum. The phenomonological rate constant, k_{obsd}, is indeed increased by addition of H_2, and as shown in Figure 12, the enhancement fits well with the form predicted by eq 21.

To extract rate parameters from the hydrogen dependence of k_{obsd}, we take the reciprocal of eq 21.

$$\frac{1}{k_{obsd}} = \frac{k_{-a}[C_2H_4]}{k_a(k_R[CO] + k_b[H_2])} + \frac{1}{k_a} \quad (22)$$

$$= \left\{\frac{k_ak_R[CO]}{k_{-a}[C_2H_4]} + \frac{k_ak_b[H_2]}{k_{-a}[C_2H_4]}\right\}^{-1} + \frac{1}{k_a} \quad (23)$$

The curve in Figure 12 is a weighted non-linear least-squares fit to the reciprocal of eq 23, using the mean values of k_a and k_R/k_{-a}, which have already been determined. The least-squares fit provides one more rate ratio for these experimental conditions: $k_{-a}/k_b = 6.2 \pm 0.7$. With the inclusion of the previous results, the following values hold when [CO] = 3.0 Torr and $[C_2H_4]$ = 400 Torr.

$$k_R/k_b = 216 \pm 27$$

$$k_{-a}/k_b = 6.2 \pm 0.7$$

This can summarized as

$$k_R:k_{-a}:k_b = 216:6.2:1$$

Thus, we can conclude that under typical hydrogenation conditions, deactivation of catalyst is fastest via CO recombination and slowest via diversion of the catalytic intermediate, $HFe(CO)_3(C_2H_5)$.

One final set of numbers is afforded by the hydrogen pressure dependence study. Gas-chromatographic product analysis at the end of the FTIR experiment reveals the total amount of ethane produced by hydrogenation. The concentration of bisethylene complex at the end of the irradiation period is obtained from the y intercept of $\ln|A - A_\infty|$ versus time plots for $Fe(CO)_3(C_2H_4)_2$ decay. Since $Fe(CO)_3(C_2H_4)_2$ builds up during irradiation and decays in the dark, this extrapolated concentration is the maximum amount of bisethylene iron tricarbonyl present during catalysis. The ratio of these two numbers provides an approximate turnover

Table II. Turnover Numbers and Turnover Rates for Ethylene Hydrogenation with Bisethylene Iron Tricarbonyl[a]

T (°C)	$[H_2]$ (Torr)	avg. $1/k_{obsd}$ (min)	$[Fe(CO)_3(C_2H_4)_2]_0$ (10^{-7} M)	$[C_2H_6]$ (10^{-5} M)	T.O.N.	T.O.R. (min^{-1})
24	300	23.3	7.28	4.99	68.5	2.94
24	506	19.2	10.4	11.1	107	5.56
24	686	16.9	11.6	12.1	104	6.15
24	700	16.3	6.72	7.82	116	7.13
24	900	14.7	6.44	10.7	166	11.3
24	900	14.1	5.04	6.85	136	9.67
43[b]	503	4.92	2.92	16.6	568	115

[a] Initial pressures: 0.10 Torr of $Fe(CO)_4(C_2H_4)$, 3.0 Torr of CO, and 400 Torr of ethylene. See text for further explanation. [b] Initial pressures: 0.050 Torr of $Fe(CO)_4(C_2H_4)$, 1.50 Torr of CO, 400 Torr of C_2H_4.

number (T.O.N.) for ethane production by $Fe(CO)_3(C_2H_4)_2$. The turnover number becomes a turnover rate (T.O.R.) when divided by the lifetime ($1/k_{obsd}$) of $Fe(CO)_3(C_2H_4)_2$. See Table II for values of T.O.N. and T.O.R. under various conditions.

These hydrogenation turnover rates are 20–60 times slower than those measured[12] for liquid-phase 1-pentene isomerization catalyzed by $Fe(CO)_3(C_2H_4)_2$ and by bis(cis-cyclooctene) iron tricarbonyl.[11] This observation fits the trend observed in our own laboratory on gas-phase $Fe(CO)_5$ photocatalyzed 1-pentene isomerization and hydrogenation. We find that isomerization is 20–40 times more efficient in its use of photons than hydrogenation.[15,30]

Kinetic Expression of the Photocatalytic Quantum Yield. We now return to the sequence of reactions comprising the catalytic system and its deactivation (Figure 13), in order to calculate the hydrogenation rate and ultimately to find an expression for the product quantum yield. Two approximations make the determination of the hydrogenation rate equation a more tractable problem. First, we average the effects of the photolysis light by defining a quantity, I_a, which is the total amount of light absorbed by the system during irradiation. The function of this light is to produce a certain total amount of bisethylene iron tricarbonyl, $[Fe(CO)_3(C_2H_4)_2]_0$, with an efficiency (or quantum yield) of ϕ. Catalytic reactions occur independently on individual iron carbonyl complexes, and substrates are present in excess, so, without loss of generality, we can adopt the convention that this total concentration is present initially. Thus at time $t = 0$

$$[Fe(CO)_3(C_2H_4)_2]_0 = \phi I_a \tag{24}$$

After time zero, the bisethylene complex decays to the monoethylene complex as detailed above. The instantaneous bisethylene concentration is

$$[Fe(CO)_3(C_2H_4)_2] = [Fe(CO)_3(C_2H_4)_2]_0 \exp(-k_{obsd}t) \tag{25}$$

where k_{obsd} is given by eq 21 (with k_b given by eq 14). During this period, hydrogenation occurs, as the decay process first takes $Fe(CO)_3(C_2H_4)_2$ to the coordinatively unsaturated catalyst, $Fe(CO)_3(C_2H_4)$.

As the second simplifying assumption, we apply the steady-state approximation to the concentration of each organometallic intermediate. This is reasonable, because intermediates are present in very small amounts, as highly reactive, non-isolable species.

To derive the rate equation, we must express the various iron carbonyls as functions of the bisethylene complex, whose concentration is known (eq 25). The mechanism of Figure 13 provides an expression for the rate of ethane production

$$d[C_2H_6]/dt = (k_3[C_2H_4] + k_4[CO])[HFe(CO)_3(C_2H_5)] \tag{26}$$

where the concentration of the intermediate, $HFe(CO)_3(C_2H_5)$, has already been derived from steady-state considerations, eq 11. For ease of manipulation, we formulate all equations making use of the composite rate constant, k_b of eq 14. Thus by inspection, $[HFe(CO)_3(C_2H_5)]$ becomes

$$[HFe(CO)_3(C_2H_5)] = \frac{k_b[H_2]}{k_4[CO]}[Fe(CO)_3(C_2H_4)] \tag{27}$$

We have already determined the steady-state value for $[Fe(CO)_3(C_2H_4)]$ (eq 16), which, upon substitution into eq 27, yields

$$[HFe(CO)_3(C_2H_5)] = \frac{k_a k_b[H_2][Fe(CO)_3(C_2H_4)_2]}{k_4[CO](k_{-a}[C_2H_4] + k_R[CO] + k_b[H_2])} \tag{28}$$

Finally, using this expression in the rate eq 26, we obtain

$$\frac{d[C_2H_6]}{dt} = \left(\frac{k_3[C_2H_4] + k_4[CO]}{k_4[CO]}\right)\frac{k_a k_b[H_2][Fe(CO)_3(C_2H_4)_2]}{k_{-a}[C_2H_4] + k_R[CO] + k_b[H_2]} \tag{29}$$

To find the rate in terms of elementary parameters, we now substitute the explicit form for k_b into the above rate equation and multiply the numerator and denominator by $\{(k_2 + k_{-1})(k_3[C_2H_4] + k_4[CO]) + k_{-1}k_{-2}\}$

$$d[C_2H_6]/dt = \{k_a k_1 k_2(k_3[C_2H_4] + k_4[CO])[H_2] \times [Fe(CO)_3(C_2H_4)_2]\}/[\{(k_2 + k_{-1})(k_3[C_2H_4] + k_4[CO]) + k_{-1}k_{-2}\}(k_{-a}[C_2H_4] + k_R[CO]) + k_1 k_2 k_4[CO][H_2]] \tag{30}$$

The rate equation predicts a direct proportionality to the concentration of bisethylene iron tricarbonyl, as we observe (see Figure 3). Ethylene and carbon monoxide pressures appear as squared terms in the denominator, indicating inhibition of the rate by these species. Ethylene inhibition is achieved by shifting the k_a, k_{-a} equilibrium away from the catalyst to the bisethylene complex. On the other hand, CO slows ethane production by irreversibly removing catalyst to the monoethylene complex by attacking both $Fe(CO)_3(C_2H_4)$ and $HFe(CO)_3(C_2H_5)$. Hydrogen appears as first-order terms in both the numerator and denominator of the rate equation. Thus the rate should increase with increasing $[H_2]$, approaching an asymptotic maximum. Rate saturation in hydrogen is expected, since this substrate initiates the catalytic cycle from a limited supply of $Fe(CO)_3(C_2H_4)$.

The product quantum yield is the total amount of ethane generated divided by the light absorbed

$$\Phi = [C_2H_6]/I_a \tag{31}$$

The total product is calculated by integration of $d[C_2H_6]/dt$ over the reaction time. We will work with the simpler form of eq 29 and substitute in the elementary form of k_b at the end. The only time-dependent term in the rate equation is the bisethylene concentration, which decays according to eq 25. Thus the rate equation is easily factored into time-independent and time-dependent parts

$$d[C_2H_6]/dt = K[Fe(CO)_3(C_2H_4)_2]_0 \exp(-k_{obsd}t) \tag{32}$$

where

$$K = \left(\frac{k_3[C_2H_4] + k_4[CO]}{k_4[CO]}\right)\frac{k_a k_b[H_2]}{k_{-a}[C_2H_4] + k_R[CO] + k_b[H_2]} \tag{33}$$

The limits of integration are from zero, when the bisethylene complex is first formed, to infinity, when it has completely reverted to monoethylene iron tetracarbonyl. Experimentally, infinite time is effectively reached after four or five $1/k_{obsd}$ lifetimes. Integration yields

$$[C_2H_6] = K[Fe(CO)_3(C_2H_4)_2]_0 \int_0^\infty \exp(-k_{obsd}t)\, dt \tag{34}$$

$$= K[Fe(CO)_3(C_2H_4)_2]_0/k_{obsd} \tag{35}$$

Substituion of K (eq 33), $[Fe(CO)_3(C_2H_4)_2]_0$ (eq 24), k_{obsd} (eq 21), and cancellation of terms yield

$$[C_2H_6] = \phi I_a\left(\frac{k_3[C_2H_4] + k_4[CO]}{k_4[CO]}\right)\frac{k_b[H_2]}{k_R[CO] + k_b[H_2]} \tag{36}$$

The quantum yield is obtained by dividing out the absorbed light.

$$\Phi = \frac{\phi(k_3[C_2H_4] + k_4[CO])}{k_4[CO]}\frac{k_b[H_2]}{k_R[CO] + k_b[H_2]} \tag{37}$$

Table III. Hydrogen-Saturated Quantum Yields and Other Derived Parameters[a]

T (°C)	$\Phi_{\infty H}$	$k_3[C_2H_4]/k_4[CO]$[b]	k_3/k_4[b]
43	54.6	160	1.2
43 (D_2)	45.2	132	0.99
32	34.1	99	0.74
23	21.0	59	0.44

[a] Initial pressures: 0.5 Torr of $Fe(CO)_5$, 3.0 Torr of CO, and 400 Torr of C_2H_4. See text for details. [b] Upper limits (see text).

Notice the rate constants k_a and k_{-a} do not appear in the quantum yield. Excess ethylene slows the rate of product formation by tying-up the catalyst as $Fe(CO)_3(C_2H_4)_2$, but all of this complex decays through formation of the catalyst, $Fe(CO)_3(C_2H_4)$, before final reversion to $Fe(CO)_4(C_2H_4)$. Thus the equilibrium represented by eq 2 and 3 affects the rate without influencing the final product yield.

Holding the ethylene and CO pressures constant, the composite rate coefficient k_b remains constant, independent of the hydrogen pressure. Thus the quantum yield (eq 37) approaches a maximum value as $[H_2]$ becomes large

$$\lim_{[H_2]\to\infty} \Phi = \frac{\phi(k_3[C_2H_4] + k_4[CO])}{k_4[CO]} \quad (38)$$

$$= \Phi_{\infty H} \quad (39)$$

The reciprocal of eq 37 provides a linearized form of the quantum yield

$$\Phi^{-1} = \frac{k_4[CO]}{\phi(k_3[C_2H_4] + k_4[CO])}\left\{1 + \frac{k_R[CO]}{k_b[H_2]}\right\} \quad (40)$$

$$= A + \frac{B}{[H_2]} \quad (41)$$

where

$$A = 1/\Phi_{\infty H} \quad (42)$$

When fit to the form of eq 41, Φ versus $[H_2]$ data such as those displayed in Figure 8 provide a value for $\Phi_{\infty H}$. Table III lists values of the hydrogen-saturated quantum yield under a variety of conditions.

Now at 337 nm the quantum yield for carbon monoxide photoejection from $Fe(CO)_4(C_2H_4)$ (eq 43) is 0.34.[31] This path leads

$$Fe(CO)_4(C_2H_4) + h\nu \xrightarrow{\phi_{CO}} Fe(CO)_3(C_2H_4) + CO \quad (43)$$

directly to the catalyst reservoir, $Fe(CO)_3(C_2H_4)_2$, by ethylene scavenging of the photoprepared $Fe(CO)_3(C_2H_4)$. Since other processes also occur during irradiation (see Figure 10), the quantum yield for bisethylene complex generation (Equation (24)) is less than 0.34. Thus by eq 38

$$\Phi_{\infty H} < (0.34)(k_3[C_2H_4] + k_4[CO])/k_4[CO] \quad (44)$$

which rearranges to

$$\frac{k_3[C_2H_4]}{k_4[CO]} > \frac{\Phi_{\infty H}}{(0.34)} - 1 \quad (45)$$

Under our usual experimental conditions, the numbers in Table III indicate $k_3[C_2H_4] \gg k_4[CO]$, so that[32]

$$k_3[C_2H_4] + k_4[CO] \simeq k_3[C_2H_4] \quad (46)$$

Then the quantum yield of eq 37 simplifies to

$$\Phi \simeq \frac{\phi k_3[C_2H_4]}{k_4[CO]} \frac{k_b[H_2]}{k_R[CO] + k_b[H_2]} \quad (47)$$

The product quantum yield can be expressed as a function solely of elementary rates by substitution of the explicit form of k_b (eq 14) into eq 37 and multiplication of top and bottom by $\{(k_2 + k_{-1})(k_3[C_2H_4] + k_4[CO]) + k_{-1}k_{-2}\}$ to clear all fractions:

$$\Phi = \{\phi k_1 k_2 (k_3[C_2H_4] + k_4[CO])[H_2]\}/[\{k_R[(k_2 + k_{-1}) \times (k_3[C_2H_4] + k_4[CO]) + k_{-1}k_{-2}] + k_1 k_2 k_4[H_2]\}[CO]] \quad (48)$$

The approximation of eq 46 yields a simpler expression which holds under our usual experimental conditions:

$$\Phi \simeq \frac{\phi k_1 k_2 k_3[C_2H_4][H_2]}{\{k_R[(k_2 + k_{-1})k_3[C_2H_4] + k_{-1}k_{-2}] + k_1 k_2 k_4[H_2]\}[CO]} \quad (49)$$

We observe the reciprocal of the quantum yield to be directly proportional to the CO pressure (Figure 6) as predicted by eq 49. The agreement is rather good, with the linear plot displaying a small, positive y intercept, which may be indicative of a low level of clustering reactions or merely due to experimental error. Experiments demonstrate that the quantum yield increases with increasing substrate (C_2H_4 and H_2) pressures to approach an asymptotic maximum. This behavior is also predicted by eq 49, which is of the form

$$\Phi = \frac{AX}{BX + C} \quad (50)$$

where X stands for either substrate. Note the quantum yield would not level off at high hydrogen pressures if $k_4 = 0$, and the only exit from the catalytic cycle was through CO recombination with the catalyst, $Fe(CO)_3(C_2H_4)$. In that case, though saturating the rate (cf. eq 30), the role of hydrogen in determining the quantum yield would be only to compete with CO reversion for the hydrogenation catalyst, making catalysis ever more efficient with increasing hydrogen pressure.

No additional insight into the deuterium isotope effect can be gleaned from eq 49. The observed ratio, $\Phi_H/\Phi_D \simeq 1.3$, is consistent with other systems in which hydride insertions play an important role.[25,29,33] The observed linear dependence of ln Φ versus $1/T$ is surprising due to the complex nature of the quantum yield and may very well not remain linear over a broader temperature range.

Summary

Irradiation of a mixture of ethylene, hydrogen, carbon monoxide, and a small amount of iron pentacarbonyl with 337-nm laser light results in the formation of ethylene-substituted iron carbonyls. Both $Fe(CO)_4(C_2H_4)$ and $Fe(CO)_3(C_2H_4)_2$ build up as a result of the absorption of near-ultraviolet light by $Fe(CO)_5$. If the initial mixture contains the monoethylene complex instead of $Fe(CO)_5$, the same final result of bisethylene iron tricarbonyl generation is obtained.

The bisethylene complex acts as a reservoir for the hydrogenation catalyst, $Fe(CO)_3(C_2H_4)$, which is formed by thermal dissociation of one highly labile ethylene. The unimolecular decay rate, k_a, is 0.17 ± 0.02 min^{-1} at room temperature, with an approximate dissociation energy of 27 ± 6 kcal/mol.

All three possible ligands (ethylene, carbon monoxide, and hydrogen) are in constant competition for the coordinatively unsaturated catalyst. Ethylene takes the catalyst back to the reservoir, $Fe(CO)_3(C_2H_4)_2$, while CO promotes irreversible conversion to the stable monoethylene complex. At room temperature, the catalyst combines 35 times faster with CO than with ethylene. However, under the usual experimental conditions of 3 Torr of CO and 400 Torr of C_2H_4, the pseudo-first-order *rate*, $k_{-a}[C_2H_4]$, is four times faster than $k_R[CO]$. Reaction with H_2 brings the catalyst into the hydrogenation cycle. Some catalyst is lost inside

(31) Miller, M. E.; Grant, E. R., unpublished results. Miller, M. E. Ph.D. Thesis, Cornell University, 1986. Established simply by measuring the quantum yield for $Fe(CO)_5$ in a CO scavanged sample of $Fe(CO)_4(C_2H_4)$.

(32) The effect of this approximation is to ignore the small contribution to product formation of the branch reaction whose rate is $k_4[CO]$ (see the mechanism in Figure 13). This asserts that for every ethane-producing loss of catalyst, by

$$HFe(CO)_3(C_2H_5) + CO \xrightarrow{k_4} Fe(CO)_4 + C_2H_6$$

many more ethylene iron carbonyls go through the catalytic cycle again. The approximation does not influence the $k_4[CO]$ contribution to catalyst reversion, which remains in the denominator of eq 49.

(33) Doi, Y.; Tamura, S.; Koshizuka, K. *J. Mol. Catal.* **1983**, *19*, 213.

the cycle by diversion of the intermediate, $HFe(CO)_3(C_2H_5)$, while much more traverses the cycle again. The ratio of recycling to reversion at the branch point, $HFe(CO)_3(C_2H_5)$, is $k_3[C_2H_4]/k_4[CO]$. This fraction is greater than 59 at room temperature and greater than 160 at 43 °C (3 Torr of CO and 400 Torr of ethylene).

As the bisethylene concentration is depleted by reversion to monoethylene iron tetracarbonyl, the catalytic hydrogenation slows, decaying to zero along with $[Fe(CO)_3(C_2H_4)_2]$. Under typical conditions, the average lifetime of the bisethylene complex (and thus of the catalysis) is 20 min at room temperature and about 3 min at 43 °C. Catalytic turnover rates per bisethylene iron tricarbonyl are on the order of 6 per minute at room temperature and 120 per minute at 43 °C.

The product quantum yield is defined as the number of ethane molecules produced per photon absorbed and provides a measure of the efficiency of the photocatalytic system. Steady-state kinetic analysis returns a rather complicated expression for quantum yield, emphasizing that even simple gas-phase organometallic catalytic systems are quite complex. Elementary rates are difficult if not impossible to obtain from this macroscopic approach. Nevertheless, the overall behavior predicted by the equations mimics the observed quantum yield results.

Only mononuclear iron carbonyls promote the catalytic hydrogenation, as indicated by the loss of quantum efficiency with increasing initial $Fe(CO)_5$ pressures. The quantum yield exhibits an inverse dependence on the carbon monoxide pressure. Reversion by CO addition to the catalyst competes more effectively with hydrogenation as the CO pressure increases.

The quantum yield rises to an asymptotic maximum with increasing ethylene and hydrogen pressures. Ethylene leveling is due to saturation of the available catalytic intermediate, $HFe(CO)_3(C_2H_5)$, in the ethane-generation step. The existence of a maximum efficiency with respect to hydrogen pressure is understood as a balance of two factors: (1) Hydrogen competes with CO for the coordinatively unsaturated catalyst, $Fe(CO)_3(C_2H_4)$. This causes the catalytic rate to increase to eventual saturation, while the quantum yield, or efficiency with respect to reversion by CO recombination, increases without bound. (2) Hydrogen initiates the catalytic cycle, one of whose intermediates occasionally exits to form the inactive monoethylene complex. This latter process, which grows in importance with increasing hydrogen pressure, provides a means by which catalytic efficiency is decreased. Deactivation by CO recombination occurs about 220 times more frequently than reversion from within the catalytic cycle, at room temperature with 3 Torr of CO plus 400 Torr of C_2H_4.

Experimental Section

Gaseous reaction mixtures are prepared on a modified Ace Glass Schlenck line with a 9 mm O-ring joint appended to each port. The only ground glass valves in the system are the three-way stopcocks on the Schlenck line. All other glassware valves are made of Teflon and fitted with Viton O-rings. A rotary pump, an oil-diffusion pump, and a liquid nitrogen cooled trap maintain a vacuum of 10^{-4} Torr or less. Compressed gas tanks are attached via stainless steel tubing and Swagelok connectors to a metal manifold, which is joined to the far end of the vacuum line. A Heise Solid Front-C-63511 Bourdon-tube pressure gauge measures pressure in the 0–1500 Torr range. An MKS Baratron Type 220B pressure gauge (capacitance manometer) reads pressures from 0 to 10 Torr with 1-mTorr accuracy. Each gauge is calibrated with a McCleod gauge of the appropriate range. Gas mixtures are prepared by the pile-on method, in which component gases are added in order of increasing final partial pressures.

All reaction cells are equipped with windows (Pyrex, quartz, CaF_2, or KBr) that transmit near-ultraviolet light. Most reactions of interest are initiated by the pulsed, unfocussed output of a Lambda Physik EMG-101 excimer laser operated on nitrogen (337 nm, 1.4 mJ pulse energy, 9 ns pulse width).

A Scientech Laser Power Meter Model 36-0001 disc calorimeter measures the attenuation of laser light by the reaction mixture. The calibrated power meter output is read by a Fluke Model 845AR high impedance voltmeter.

Product analysis experiments follow the transformation of ethylene to ethane in the active catalytic hydrogenation system on an F&M Scientific Model 810-19 gas chromatograph. The reactants are mixed in 10 cm long/5 cm diameter cylindrical Pyrex cells fitted with Pyrex windows. Each cell contains two stopcocks in series, separated by a very small section of glass tubing, which permits the transfer of small aliquots of the reacting system to the GC. A loaded cell is irradiated while resting in a 1 in. thick aluminum cradle which is wrapped with heating tape to maintain a constant temperature within the range of 22–70 °C. See Figure 14a for a diagram of this irradiation setup.

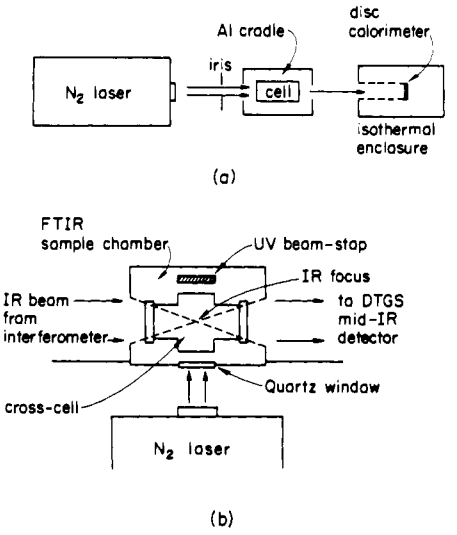

Figure 14. The photolysis setup for (a) product analysis experiments and (b) FTIR experiments.

Reactant aliquots are swept into the GC column by a 50 psi backpressure of helium carrier gas. The 10 ft. × $^1/_8$ in. salt-modified alumina column is prepared by the method of Sawyer and Brookman[34] to maximize the difference in retention time between saturated and unsaturated hydrocarbons. Acid-washed alumina is washed with sodium sulfate to provide a 10% by weight coating. The dried material is then sieved to provide the column packing with particles in the 125–150 μm range.

The column is operated at 110 °C with a 50 psi helium inlet pressure. Under these conditions ethane elutes after 4.5 min and ethylene after 5.5 min as detected by flame ionization. Ethane and ethylene exhibit full-widths-at-half-maximum of 9 and 15 s, respectively. Equal amounts of ethane and ethylene give identical peak areas as measured by triangulation.

Fourier transform infrared (FTIR) spectra are measured on an IBM FTIR spectrometer (Model IR/98). To allow in situ laser irradiation of the FTIR sample, the spectrometer is fitted with a special removable aluminum side plate equipped with a 2 × $^1/_8$ in. quartz window. The UV window is located so that the unfocussed laser light passes at right angles through the focal point of the FTIR beam inside the sample chamber. The arrangement is illustrated in Figure 14b.

For each experiment, a reference spectrum of the evacuated sample cell is recorded, against which the absorbance spectra are calculated. The IBM IR/98 also provides spectral subtraction and base line linearization capabilities.

Infrared cells are constructed from 1.825 in. outer diameter Corning Pyrex Conical tubing. Three-piece aluminum removable window clamps hold infrared windows to either end with Viton O-ring seals. For in situ laser irradiation, a cross-cell and a T-cell contain Pyrex or quartz windows on an axis perpendicular to the IR axis.

To perform elevated temperature experiments, the T-cell is wrapped with heating tape whose leads are connected to an RFL Industries proportional temperature controller (Model 70A). A chromel–alumel thermocouple with an ice–water reference provides accurate temperature measurement (±0.2 °C).

Hydrogen is Matheson UHP (99.999% min). Research grade carbon monoxide (99.99% min) is also obtained from Matheson. UHP grade deuterium (Cryogenic Rare Gas) contains no detectable air (<0.0004%) and 1.44% H_2 and HD. The H_2, D_2, and CO are used as received. Portions of Matheson C. P. grade ethylene (99.5% min) are purified by three liquid nitrogen cooled freeze–pump–thaw cycles prior to use.

Iron pentacarbonyl (Strem) is first outgassed by 3 freeze–pump–thaw cycles. The orange liquid is then vacuum transferred to a Schlenck tube containing a few milliliters of 4 Å molecular sieves, which has been dried under vacuum for 4 h at 125 °C. Iron pentacarbonyl is stored over dry

(34) Sawyer, D. T.; Brookman, D. J. *Anal. Chem.* **1968**, *40*, 1847.

ice (-78 °C) in the dark to slow down clustering reactions such as eq 51 and 52.

$$2Fe(CO)_5 \rightarrow Fe_2(CO)_9 + CO \quad (51)$$

$$Fe(CO)_5 + Fe_2(CO)_9 \rightarrow Fe_3(CO)_{12} + 2CO \quad (52)$$

Prior to each use, $Fe(CO)_5$ is opened to the vacuum several times to remove any evolved CO.

Ethylenetetracarbonyliron is synthesized by the method of Murdoch and Weiss.[35] The 300-mL cannister of a Parr pressure reactor is loaded in an argon-purged glovebox with 50 g of $Fe_2(CO)_9$ (Strem) and 125 mL of pentane which has been distilled over sodium benzophenone. The cannister is pressurized to 750 psi with Matheson Research grade ethylene (99.99% min) and stirred at room temperature for 2 days. Periodically, the canister is repressurized to 750 psi as ethylene dissolves and reacts according to eq 53. The resultant green-brown liquid is

$$Fe_2(CO)_9 + C_2H_4 \rightarrow Fe(CO)_4(C_2H_4) + Fe(CO)_5 \quad (53)$$

degassed and most of the pentane is evaporated away. The remaining liquid is fractionally distilled to an icewater cooled receiving flask under a reduced pressure of 10 Torr. The first fraction is $Fe(CO)_5$, which is collected between 24 and 28 °C. The second fraction, collected from 28 to 33 °C, is a yellow-orange mixture of $Fe(CO)_5$ and $Fe(CO)_4(C_2H_4)$. The final fraction is yellow $Fe(CO)_4(C_2H_4)$, which is collected between 32 and 34 °C. This final fraction is thoroughly degassed, transferred to a clean, dry Schlenck tube, and stored over dry ice in the dark. No $Fe(CO)_5$ is detected in the final product by FTIR.

Over time, $Fe(CO)_4(C_2H_4)$ decomposes by forming dodecacarbonyltriiron and ethylene as illustrated in eq 54.

$$3Fe(CO)_4(C_2H_4) \rightarrow Fe_3(CO)_{12} + 3C_2H_4 \quad (54)$$

Thus, $Fe(CO)_4(C_2H_4)$ is opened to the vacuum several times before each use, to remove any free ethylene.

Acknowledgment. This work was supported by the National Science Foundation under Grant No. CHE-86 14702.

Registry No. $CH_2{=}CH_2$, 74-85-1; $Fe(CO)_3(C_2H_4)_2$, 74278-01-6.

(35) Murdoch, H. D.; Weiss, E. *Helv. Chim. Acta* **1963**, *46*, 1588.

Molecular Modeling of Zeolite Structure. 1. Properties of the Sodalite Cage

M. Mabilia,[†] R. A. Pearlstein,[‡] and A. J. Hopfinger*[‡§]

Contribution from Intersoft Inc., Lake Forest, Illinois 60045, and Department of Medicinal Chemistry and Pharmacognosy and Department of Chemistry, University of Illinois at Chicago, Chicago, Illinois 60680. *Received February 9, 1987*

Abstract: Free-valence geometry molecular mechanics calculations were carried out on a sodalite cage. Energy minimizations were performed as a function of cage oxygen geometry, flexibility of the surface hydroxyl groups, Si:Al composition and bonding topology, and choice of force-field parameters. The major finding is that incorporation of Al atoms into the sodalite cage has little effect on the optimized molecular geometry, but plays a major role on structural stability. As the amount of Al increases, the stability of the sodalite cage also increases. For a fixed Si:Al composition, bonding topologies having localized high density groupings of Al atoms form more stable sodalite cages than those built from random or uniform distributions of Al atoms. Al atoms also increase the ionic character of the sodalite cage. Unique framework oxygen geometries which maximize the stability of a sodalite cage were identified. The optimized sodalite cage structures located on the surface of a zeolite were found to be virtually the same as those within a zeolite framework. Mobile ion-binding calculations, using Na^+ and K^+, indicate that ion-binding strength is most dependent upon the geometry of the cage oxygens. Al atoms play a relatively minor role in ion-binding energetics and specificity.

Zeolites are framework structures usually composed of aluminum, silicon, and oxygen.[1] The zeolite frames constitute porous networks having molecular dimensions. The particular size, shape, and dimensionality of the pores can be controlled by atomic composition and synthetic conditions. Thirty-nine different framework topologies have been observed to date for aluminosilicate zeolites.

Zeolites are increasingly being used in three major commercial applications: catalysis, selective ion exchange, and as molecular sieves and sorbents. Each of these important applications is due to a different component of zeolite structural chemistry. The structural networks in zeolites constitute selective substrates for mobile, nonframework cations, hence the useful ion-exchange properties. The micropores of zeolites are hydrophilic to organophilic depending upon atomic composition. These pores can also be of controlled size(s) and accessibility. Overall, these properties make zeolites effective as sorbents and molecular sieves. The high polarity of bonded atoms in zeolites results in molecular surfaces having highly active sites, again of controlled dimensions. This makes zeolite materials useful in selective catalysis.

At first glance the structural characterization of zeolites would seem straightforward, given their crystalline nature. Unfortunately, these materials have complex bonding topologies and large unit cells. Since diffraction methods yield only a composite average view of a structure, local structural features of zeolites are difficult to discern. Different zeolites can contain common building block structures, additionally making structural differentiation difficult. Perhaps the most significant limitation in applying X-ray diffraction until recently is the small size of synthetic zeolite crystals, normally less than 5 μm in average dimension. Thus, powder diffraction analyses have been the conventional means of distinguishing different zeolites, and, to a lesser extent, determining zeolite structure.[2] However, the loss of structural information inherent to powder diffraction data is usually sufficient to negate detailed refinement of zeolite framework structures.

The net result of these drawbacks and limitations to apply X-ray diffraction methods for the structural resolution of zeolites has

[†] Intersoft Inc.

[‡] Department of Medicinal Chemistry and Pharmacognosy, University of Illinois.

[§] Department of Medicinal Chemistry and Pharmacognosy and Department of Chemistry, University of Illinois.

(1) Newsam, J. M. *Science* **1986**, *231*, 1093.

(2) Barri, S. A. I.; Smith, G. W.; White, D.; Young, D. *Nature (London)* **1984**, *312*, 533.

0002-7863/87/1509-7960$01.50/0